LA-UR-15-22667 (Accepted Manuscript)

# Ionospheric acoustic and gravity waves associated with midlatitude thunderstorms

Lay, Erin Hoffmann
Shao, Xuan-Min
Kendrick, Alexander Kent
Carrano, Charles S

Provided by the author(s) and the Los Alamos National Laboratory (2016-04-08).

**To be published in:** Journal of Geophysical Research: Space Physics

**DOI to publisher's version:** 10.1002/2015JA021334

**Permalink to record:** http://permalink.lanl.gov/object/view?what=info:lanl-repo/lareport/LA-UR-15-22667

**Disclaimer:**
Approved for public release. Los Alamos National Laboratory, an affirmative action/equal opportunity employer, is operated by the Los Alamos National Security, LLC for the National Nuclear Security Administration of the U.S. Department of Energy under contract DE-AC52-06NA25396. Los Alamos National Laboratory strongly supports academic freedom and a researcher's right to publish; as an institution, however, the Laboratory does not endorse the viewpoint of a publication or guarantee its technical correctness.

# Ionospheric acoustic and gravity waves associated with mid-latitude thunderstorms

Erin H. Lay[1], Xuan-Min Shao[1], Alexander K. Kendrick[1], Charles S. Carrano[2]

[1]Space and Remote Sensing Group, Los Alamos National Laboratory, Los Alamos, New Mexico, USA

[2]Institute for Scientific Research, Boston College, Boston, MA, USA

Corresponding Author:

Erin H. Lay

Space and Remote Sensing Group, ISR-2, MS D436

Los Alamos National Laboratory

Los Alamos, NM 87545, USA

elay@lanl.gov

**Abstract:**

Acoustic waves with periods of 2 - 4 minutes and gravity waves with periods of 6 - 16 minutes have been detected at ionospheric heights (250-350 km) using GPS Total Electron Content (TEC) measurements. The area disturbed by these waves and the wave amplitudes have been associated with underlying thunderstorm activity. A statistical study comparing NEXRAD radar thunderstorm measurements with ionospheric acoustic and gravity waves in the mid-latitude U.S. Great Plains region was performed for the time period of May - July 2005. An increase of ionospheric acoustic wave disturbed area and amplitude is primarily associated with large thunderstorms (mesoscale convective systems). Ionospheric gravity wave disturbed area and amplitude scale with thunderstorm activity, with even small storms (i.e. individual storm cells) producing an increase of gravity waves.

## Introduction:

Recent scientific interest has focused on the effect of tropospheric weather (below ~12 km) on the ionospheric plasma distribution [Vadas and Fritts, 2004; Immel et al., 2009; Kumar et al., 2009a; 2009b]. Thunderstorm-originated atmospheric gravity waves with periods longer than ~5 minutes have been observed in the ionospheric F-region (200-400 km) [Lay et al., 2013; Vadas and Liu, 2013] and at lower D-region altitudes (80-100 km) [Yue et al., 2009; Lay and Shao, 2011a, 2011b; Yue et al., 2013]. The source of these gravity waves is typically thought to be the overshooting of convective thunderstorm plumes [Vadas and Fritts, 2004]. The ionospheric plasma responds to the neutral gravity waves, as is evidenced by wave structures detected in the electron density. Dynamical processes, photoionization, chemical loss processes, and filtering by atmospheric winds are all instrumental in the coupling between neutral waves and the ionospheric response [Hooke, 1968; Ding et al., 2003]. In this paper, we refer to the ionospheric response at gravity wave frequencies as ionospheric gravity waves (IGWs).

Shorter period (1 – 4.5 min; 3.7 – 16.7 mHz) wave variations associated with severe thunderstorms have also been observed in the F-region [Georges 1968; Baker and Davies, 1969; Lay et al., 2013] and D-region [Marshall and Snively, 2014]. Model results of acoustic wave propagation are consistent with observations, and indicate that such waves originating from thunderstorm heights (< 12 km) should be able to reach 250-350 km altitude within ~250 km horizontally of the source [Walterscheid et al., 2003; Zettergren and Snively, 2013]. The thermospheric

temperature gradient acts as a cutoff for acoustic waves with period greater than ~4.5 minutes, preventing lower frequency acoustic waves from propagating to the ionosphere [Georges 1968; Walterscheid et al., 2003]. Although modeling indicates that acoustic waves should reach ionospheric heights, the source for such waves is still unclear. While models typically use thunderstorm convection as the source, such a mechanism has not been confirmed. In addition, the atmospheric cutoff at lower frequencies makes it unclear whether the source is a narrowband emitter, or whether it is a broadband emitter that is filtered as it propagates into the ionosphere. In this paper we refer to the ionospheric plasma response to atmospheric acoustic wave frequencies as ionospheric acoustic waves (IAWs).

Ground-based infrasound acoustic waves in the frequency range of 0.01 – 10 Hz have been measured from thunderstorms for decades [Bowman and Bedard, 1971]. Among those observations, infrasound waves have been associated with tornadic storms [Bedard, 2005], and more recently, from electrical discharges called sprites [Farges et al., 2005; Farges and Blanc, 2010]. Infrasound waves from intense convection associated with tornados would have a source region at cloud height, ~5-12 km altitude. Sprites occur at 75-85 km altitude above multi-cell, long duration thunderstorms called mesoscale convective systems (MCS) [Lyons et al., 2000; 2008]. These MCS are typically larger than 100 km in at least one lateral direction, and last for more than 6 hours. Ground-based infrasound measurements detect acoustic waves associated with thunderstorms that are ducted between the ground and thermospheric temperature gradient at ~100-110 km altitude. Acoustic waves that reach the ionosphere are likely from the same source as those detected

on the ground, but have not been refracted downward upon reaching the thermospheric temperature gradient. The temperature gradient around 100-120 km altitude also acts as a filter, only allowing the lower frequency acoustic waves through to the ionosphere [Walterscheid et al., 2003]. Thus, it is possible that it is easier for acoustic waves generated at higher altitudes, such as from sprites, to propagate through the gradient without as much loss.

The goal of this report is to provide a better understanding of the source of IAWs and IGWs by associating thunderstorm characteristics with the occurrence of large amplitude ionospheric acoustic and gravity waves via a 3-month statistical study. The increasing numbers of Global Positioning System (GPS) ground-based receivers in the U.S. Great Plains now allows nearly full spatial and temporal coverage of ionospheric waves above thunderstorms in that region for the first time.

**Data Processing: GPS TEC measurements**

The dispersive contributions to L1 and L2 GPS signals (1.58 and 1.22 GHz, respectively) detected by GPS ground receivers are used to calculate the integrated electron density from satellite to receiver, or total electron content (TEC) [Burrell et al., 2009; Seemala and Valladares, 2011]. TEC is determined by a combination of the rough but absolute pseudorange measurement and the precise but ambiguous phase differential measurement (phase TEC). The TEC measurements have been converted to vertical TEC (VTEC) values by dividing them by the single layer mapping function, $\mathrm{M}(\varepsilon, h) = \sec\left[\sin^{-1}\left(\frac{R_e \cos\varepsilon}{R_e + h}\right)\right]$ where $R_e$ is the Earth radius, $\varepsilon$ is

the satellite elevation angle, and *h* is the ionospheric height, assumed to be 350 km [Seemala and Valladares, 2011].

In order to sensitively detect TEC perturbations, VTEC is detrended by subtracting a best-fit polynomial (Fig. 1a,b) [Lay et al., 2013]. This process removes the gross offset, and the detrended result is mostly related to the phase TEC (0.01 – 0.1 TECU accuracy [Burrell et al., 2009]). The remaining residual represents the higher frequency variations along the measurement path. For ionospheric acoustic waves, we then apply a band-pass filter for frequencies between 4.2 and 8.3 mHz (2 – 4 minute periods) (Fig. 1c). The analytic signal amplitude envelope of the bandpass-filtered signal is computed (Fig. 1d), and any perturbations that exceed a given threshold for longer than 4 minutes are marked as ionospheric acoustic waves (red overlay, Fig. 1c). In this paper, a 0.025 TECU threshold was chosen for IAWs to be above the general noise level (~0.02 TECU) of the signal. For IGWs, the signal is bandpass filtered between 1.0 and 2.8 mHz (6 – 16 minute periods) with an amplitude threshold of 0.08 TECU.

**Data processing: statistical study**

To provide a better understanding of the connection between thunderstorms and ionospheric acoustic waves, we perform a study that compares GPS-TEC-measured IAWs with thunderstorm size determined by NEXRAD radar measurements. The region of study is the mid-latitude U.S. Great Plains region from -108° to -90° East and 33° to 42° North (Figure 2), from May – July 2005. Thunderstorm size was determined every 10 minutes from radar reflectivity

measurements in this region from eight National Weather Service NEXRAD WSR-88D radars (http://www.roc.noaa.gov/WSR88D/). The reflectivity is associated with the intensity of the thunderstorm, with reflectivity > 30 dBZ indicative of precipitation-sized ice [Wiens et al., 2008]. The metric we define for thunderstorm area, $A_{30dBZ}$, is determined by the area of the number of 20 x 20 km grid boxes with a maximum reflectivity > 30 dBZ. This maximum reflectivity value is the maximum for all altitudes measures (~5-12 km), and not at a specific altitude level. A complete description of the processing of the radar data is found in Wiens et al. [2008].

For comparison to thunderstorm size, we calculated IAW wave area (AIAW) and IAW maximum amplitude every 10 minutes. We calculated IGW wave area (AIGW) and IGW maximum amplitude every 30 minutes, to allow for the 16-minute maximum IGW wave period. These quantities were determined using TEC measurements along lines of sight from 61 Continuously Operating Reference Station (CORS; http://geodesy.noaa.gov/CORS/) Network GPS ground receivers (listed in Table S1 of Supporting Information) to all visible GPS satellites. Each satellite/station pair was searched for data arcs longer than 1 hour. We excluded data for which the line-of-sight had an elevation angle less than 30°. For each arc, the wave amplitude was calculated (Fig. 1d), and the maximum amplitude in 40-km x 40-km x 10-minute grid boxes was saved for IAWs, and in 40-km x 40-km x 30-minute grid boxes for IGWs. The larger grid box size, as compared to the thunderstorm grid box, is used based on lower spatial accuracy due to conversion from slant TEC to VTEC and due to satellite motion during each 10-minute window. The spatial grid is shown in Figure 2a. If multiple arcs passed through the same grid

box, the median of the maximum amplitudes from all arcs in the box was calculated. If no data arcs passed through a given grid box, then that box was recorded as 'unsampled'.

Because acoustic waves will propagate asymmetrically away from the source, dependent on wind and magnetic field direction [Zettergren and Snively, 2013], we do not compare thunderstorm spatial grid boxes directly to ionospheric spatial grid boxes to determine the statistical relationship between thunderstorm and ionospheric waves. Instead, metrics from the whole study region are used. The metric used to measure thunderstorm size is the effective area of the thunderstorm within the spatial grid with reflectivity higher than 30 dBZ ($A_{30dBZ}$). Ionospheric wave response is measured by area and amplitude.

Ionospheric wave area is the primary metric used to measure the ionospheric response to thunderstorms. However, since every spatial grid box is not sampled for every time interval due to the time and spatial dependence of GPS TEC satellite/receiver arcs and the density of the GPS receiver stations, we define a "scaled area" (Figure 2b). For a given 10-min time period, N grid boxes are sampled by GPS measurements. Of those, NW boxes surpass the wave threshold (0.025 TECU for IAW and 0.08 TECU for IGW). The fraction of the sampled grid with waves is then NW/N. To get the scaled area, the fraction is multiplied by the entire grid area, $A_g$: scaled area = $A_g$(NW/N). This scaled area is named $A_{IAW}$ for IAW scaled area and $A_{IGW}$ for IGW scaled area.

The secondary ionospheric metric we use is maximum wave amplitude, defined as the maximum wave amplitude over the whole study area for each 10 minutes (30 minutes for IGWs). This metric shows the general magnitude of perturbations, but is only used as a secondary metric since its value is highly dependent on where the wave is measured relative to the source location (Figure 2c). Since the GPS TEC arcs do not measure all points on the study grid for each time period, it is possible that the wave maximum might not be measured, skewing the maximum amplitude on the low side. Therefore, we feel that the scaled area covered by ionospheric waves is a more stable measurement of the ionospheric perturbations, and should be used as the primary metric.

It is expected that periods of high geomagnetic activity will have significant ionospheric perturbations associated with the geomagnetic activity. For this reason, we use the Kp-index, a standardized 3-hour planetary geomagnetic activity index to monitor the level of geomagnetic activity. The Kp data are available at http://spidr.ngdc.noaa.gov/spidr/). For all statistical averages in this paper (Figures 5 & 7), measurements on days in which the Kp exceeded 5.3 were excluded.

## Results: Case Studies

Figure 3 shows two individual case studies of the location and extent of ionospheric acoustic waves (left column) and ionospheric gravity waves (right column). To avoid too much clutter on the plot, not every receiver/satellite arc is shown. Instead, a subset of 41 stations is chosen (bold blue highlighting, Suppl.

Materials, Table 1) with lines of sight to GPS satellites PRN 1, 20, and 25. Light gray lines show the entire satellite-to-receiver arc projected to 350-km altitude. Red points show locations with ionospheric wave variations larger than threshold (0.025 TECU for IAW, 0.08 TECU for IGW) in amplitude. Black/gray contours show lightning density within the same time period as measured by the Los Alamos Sferic Array [Shao et al., 2006; Wiens et al., 2008], with the contour levels representing 2.5 (lightest), 4.5, 6.5, and 8.5 (darkest) lightning events/km$^2$.

Fig. 3a shows a map of IAWs detected between 2100 – 0200 UTC (1600 – 2100 local time) on 9 – 10 June 2005. This figure shows strong ionospheric acoustic waves located nearby the most lightning-intense thunderstorm regions. Figure 3b shows similar results for another example from 2100 – 0100 UTC 16 – 17 June 2005. However, the region covered by acoustic waves is slightly smaller and the region with high thunderstorm activity is smaller as well. The right column of Figure 3 maps the IGWs detected near those same two thunderstorms. Figure 3c shows that IGWs cover a greater fraction of the entire region than IAWs, but are more dispersed than acoustic waves. Figure 3d shows a similar result, but for the smaller thunderstorm.

**Results: Statistical Study**

The black curve in Figure 4 shows $A_{30dBZ}$, the effective thunderstorm area (in thousands of km$^2$) with reflectivity higher than 30 dBZ over the 3-month period of the statistical study. $A_{IAW}$ (IAW scaled area; lower gray curve) and $A_{IGW}$ (IGW scaled

area; upper gray curve) are also plotted during the same time period, scaled relative to $A_{30dBZ}$ by a factor of 10. $A_{IGW}$ has been offset vertically from $A_{IAW}$ by 400,000 km$^2$. Shaded areas show time periods with high geomagnetic activity (Kp > 5.3). During time periods with medium to low geomagnetic activity, $A_{IGW}$ and $A_{IAW}$ track $A_{30dBZ}$ relatively well. Other than during periods of high geomagnetic activity in this study, time periods with significant ionospheric waves in the frequency range studied here are rarely observed without associated thunderstorm activity.

To more clearly see relationships between thunderstorm activity and ionospheric response, we show diurnal averages of the data from Figure 4. Figure 5 shows the diurnal averages of thunderstorm area (top row), ionospheric wave scaled area (middle row), and maximum wave amplitude (bottom row) for IAWs (left column) and IGWs (right column). Time starts at 1200 UTC (0600 local standard time) to best show the increased thunderstorm activity in late afternoon/evening local time. Days with a maximum Kp > 5.3 have not been included in the averages. The blue curves show the diurnal average of only those days with high thunderstorm activity (maximum $A_{30dBZ}$ > 40,000 km$^2$). The red curves show the diurnal average of days with low thunderstorm activity (maximum $A_{30dBZ}$ < 10,000 km$^2$). The black curve shows the diurnal average for low thunderstorm activity days, but excludes 18 June and 30 July, as will be discussed below. The high thunderstorm activity average (blue) includes 17 days. The low thunderstorm average (red) includes 14 days.

The diurnal behavior of the thunderstorm area (top row) is expected due to late afternoon heating of land masses. The red and black curves in the top row have been multiplied by 10 to more easily see the diurnal variation on days with low thunderstorm activity. Figures 5a and 5d show the same results: Figure 5a uses the 10-minute bin for comparison to IAW behavior, while Figure 5d uses the 30-minute bin for comparison to IGW behavior.

Diurnal IAW area and maximum amplitude variations on days with high thunderstorm activity are shown in blue in Figure 5b and c, respectively. Diurnal IAW area shows a peak for days with high thunderstorm activity that is similar in shape to the diurnal thunderstorm variation, slightly after the thunderstorm peak (Fig. 5b, blue curve). The peak of the blue curve in 5c also occurs at generally the same time, indicating that the maximum IAW amplitude follows a similar pattern on days with high thunderstorm activity. The maximum amplitude is less smooth in general since the measured amplitude depends significantly on where the wave is measured relative to the source of the disturbance. Nevertheless, a general trend of increased wave amplitude is visible on high thunderstorm activity days.

Diurnal averages of the days with low thunderstorm activity show peaks between 0200 – 0500 UTC in the red curves of Figure 5b and c. This peak is several hours after the peak in the thunderstorm activity, suggesting that these IAWs are unrelated to thunderstorm behavior on days with low thunderstorm activity, and are most likely associated with a different source. In fact, the major contribution from those peaks comes from just two days, June 18 and July 30. The black curves

show averages for low thunderstorm activity days with June 18 and July 30 removed. Removing those days from the averages does not change the diurnal thunderstorm behavior (red vs black curves in Fig. 5a), but it does significantly change the ionospheric response (Fig. 5 b-c). The black curves in Figure 5 b-c show no significant diurnal pattern. This suggests that when the thunderstorm area is less than 10,000 $km^2$, there are no statistically observable acoustic waves associated with thunderstorms. The acoustic waves between 0200 – 0500 UTC on June 18 and July 30 are most likely associated with some other phenomenon. A possible source of IAWs could be extraterrestrial objects that produce a shock wave upon entry to the atmosphere, such as meteors. July 29 - 30 is the peak of the alpha-Capricornid meteor shower that is known for producing fireballs [Wright et al., 1956]. In fact, two fireballs were reported over the U.S. during the time of the $A_{iaw}$ peak (http://www.amsmeteors.org/members/fireball/browse_reports). A future study will report on the ionospheric response to meteors and fireballs.

The right column of Figure 5 shows results of the same type of analysis for gravity waves. Figure 5e shows a similar diurnal variation for low and high thunderstorm activity days, with the peak magnitude of the variation being significantly larger on days with high thunderstorm activity (300,000 km2 vs. < 90,000 $km^2$). The same trend is visible in Figure 5f for the maximum IGW amplitude.

In general, Figure 5 indicates that IAW area and amplitude are detectably larger on days with high thunderstorm activity, but have no statistically significant deviations on days with low thunderstorm activity, excluding June 18 and July 30.

Gravity wave area and amplitude increase on days with high thunderstorm activity, and still exist with smaller magnitudes on days with lower, but non-zero, thunderstorm activity.

Next, in Figure 6, we use the data from Figure 4 to produce scatter plots of ionospheric response versus thunderstorm area for each 10-minute period. The total number of data points in each $A_{30dBz}$ bin is plotted in Figure 6a to show the statistics. Figure 6b shows ionospheric acoustic wave area ($A_{IAW}$) versus thunderstorm area. Figure 6c shows the maximum amplitude of the ionospheric acoustic wave versus thunderstorm area. Figure 6d shows $A_{IGW}$ versus thunderstorm area, and Figure 6e shows the maximum amplitude of the ionospheric gravity wave versus thunderstorm area. 10-minute periods with Kp> 5.3 are highlighted with red diamonds. 10-minute periods with more than 20 positive cloud-to-ground lightning (+CGs) as determined by LASA are highlighted with blue squares. +CGs with peak current less than 20 kA were removed from the counts, as those could be positive in-cloud events mistakenly labeled as +CG.

The red diamonds in Figures 6b-e show that the majority of events with large IAW or IGW perturbations and small thunderstorm areas are accounted for by enhanced geomagnetic activity. The blue squares in Figures 6b-e show 10-minute time periods likely to be associated with sprites and large MCS stratiform regions. Because of the large number of counts at lower thunderstorm area, and smaller number of counts at higher areas (Figure 6a), it is more illuminating to normalize

these plots by the total number of counts per thunderstorm area to separate noise from signal.

Figure 7 shows a 2-D normalized histogram of thunderstorm area versus $A_{IAW}$ (Fig. 7a), maximum IAW amplitude (Fig. 7b), $A_{IGW}$ (Fig. 7c), and maximum IGW amplitude (Fig. 7d). The normalized histogram accounts for the fact that there are far more time periods with smaller $A_{30dBZ}$ than with large $A_{30dBZ}$ as follows: data from each 10-minute time period is binned by $A_{30dBZ}$ (horizontal axis), and all data in each $A_{30dBZ}$ bin is used to generate a histogram in wave area (vertical axis). Then the histogram is divided by the total number of boxes in the given $A_{30dBZ}$ bin to normalize for occurrence frequency. $A_{30dBZ}$ horizontal bins have variable width in order to generate enough statistics in the bins on the far right of the plots. Results for ionospheric acoustic waves ($A_{IAW}$ and maximum IAW amplitude) versus thunderstorm area are shown in the left column of Figure 7, while ionospheric gravity wave results ($A_{IGW}$ and maximum IGW amplitude) versus thunderstorm area are shown in the right column.

In general, $A_{IAW}$ increases as the thunderstorm area increases, only consistently exceeding the noise background when A30dBZ > ~45,000 km$^2$. Figure 7b shows that the IAW amplitude starts increasing significantly for thunderstorms with areas larger than ~40,000 km$^2$. $A_{IGW}$ (Fig. 7c) and IGW maximum amplitude (Fig. 7d) also increase significantly when the thunderstorm area exceeds ~40,000 km$^2$. However, this relationship is not exclusive: there are some time periods with smaller thunderstorm area but still significant IGW activity and amplitudes.

## Summary and Discussion

We study the ionospheric response to thunderstorms at acoustic and gravity wave frequencies. Our findings show that thunderstorms are a main driver of mid-latitude IAWs and IGWs during low to mid-geomagnetic activity. Initial case studies show that the areas disturbed by IAWs and IGWs increased as thunderstorm activity increased. In addition, the majority of 2 – 4 minute ionospheric acoustic fluctuations in the mid-latitude U.S. Great Plains are associated closely in space and time with thunderstorms. The statistical study presented in this report confirms the case study findings. Diurnal averages of IAWs and IGWs of days with high thunderstorm activity showed significantly larger disturbed wave areas (typically > 200,000-300,000 $km^2$) than averages of low thunderstorm activity days (<100,000 $km^2$).

An interesting feature of the diurnal averages in Figure 5b and 5e is that the ionospheric waves seem to damp out before the thunderstorm activity dies down. Figure 8 shows vertical TEC curves for the days of the statistical study in black and their average in red. This plot shows that the daily TEC decreases between 0300 and 0600 UTC to its nighttime value. The IAW and IGW areas from Figure 5 also damp out in this time window. We suggest that changes corresponding with the nighttime ionosphere, such as less plasma at lower altitudes (<350 km), no new ionization, and slower recombination rates, leads to the observed damping of IAWs and IGWs [Hooke, 1968; Ding et al., 2003]. Although a complete coupling study is beyond the scope of this paper, it seems clear that fewer thunderstorm-associated

perturbations are detected at nighttime than daytime despite strong thunderstorm activity.

The statistical study in this report shows that, while ionospheric gravity waves do have larger amplitudes and disturbed areas for MCS-type thunderstorms, they are also prevalent above smaller, single-celled thunderstorms. The gravity wave findings are consistent with the theory of generation of gravity waves from overshooting cloud tops [Vadas and Fritts, 2004]. It is possible to have a single-celled thunderstorm with a strong convective core that overshoots the tropopause, generating gravity waves. Mesoscale convective systems will have several convective cells that can overshoot the tropopause, thus generating more gravity waves. This study also suggests that an upper bound for the average IGW fluctuation above a nearby thunderstorm is ~0.6 TECU.

In comparison, ionospheric acoustic waves occur preferentially over thunderstorms with large areas (> 25,000 $km^2$) of reflectivity higher than 30 dBZ (Fig. 7a,b) that also have a significant number of +CG lightning. Smaller storms have relatively little acoustic wave activity. Because storms with large areas and lots of +CG lightning typically have large stratiform regions, this finding suggests that the majority of IAWs may be from a source that is also associated with the large stratiform region, such as sprites or large horizontal “spider” lightning associated with +CG lightning in MCS thunderstorms. A higher source region, such as from sprites, would make it easier for the acoustic wave to penetrate the lower thermosphere into the ionosphere, but this study is unable to discriminate between

the two possibilities. The findings in this paper do not rule out intense convection as a source of ionospheric acoustic waves, but they suggest that it is not the primary generation method.

**Acknowledgements**

This research was supported by the Los Alamos National Laboratory's Laboratory Directed Research and Development (LDRD) project 20130737ECR. Ground-based GPS receiver data used in this study was downloaded from http://geodesy.noaa.gov/CORS/. NEXRAD radar data was downloaded from http://www.roc.noaa.gov/WSR88D/. Los Alamos Sferic Array data used in the analysis can be released through official Los Alamos National Laboratory's release policy after a request is made to authors E H L or X-M S.

## References


Baker, D. M. & Davies, K. (1969), *F2*-region acoustic waves from severe weather, *J. of Atmos. and Terr. Phys.*, *31*, p 1345-1352.

Bedard, A. J. (2005), Low-Frequency Atmospheric Acoustic Energy Associated with Vortices Produced by Thunderstorms, *Monthly Weather Rev. 133* (1), 241 – 263.

Bowman, H. S. and A. J. Bedard (1971), Observations of Infrasound and Subsonic Disturbances Related to Severe Weather*, Geophys. J. R. Astr. Soc., 26*, 215-242.

Burrell, A. G., Bonito, N. A. & Carrano, C. S. (2009), Total electron content processing from GPS observations to facilitate ionospheric modeling, *GPS Solutions*, *13*(2), doi:10.1007/s10291-008-0102-3.

Ding, F., W. Wan, and H. Yuan (2003), The influence of background winds and attenuation on the propagation of atmospheric gravity waves, *J. of Atmos. and Terr. Phys., 65*, 857-869.

Farges, T., and E. Blanc (2010), Characteristics of infrasound from lightning and sprites near thunderstorm areas, *J. Geophys. Res., 115*, A00E31, doi:10.1029/2009JA014700.

Farges, T., E. Blanc, A. Le Pichon, T. Neubert, and T. H. Allin (2005), Identification of infrasound produced by sprites during the Sprite2003 campaign, *Geophys. Res. Lett., 32*, L01813, doi:10.1029/2004GL021212.

Georges, T. M. (1968), HF Doppler studies of traveling ionospheric disturbances, *J. of Atmos. and Terr. Phys.*, *30*, 735-746.

Hooke, W. H. (1968), Ionospheric irregularities produced by internal atmospheric gravity waves, *J. of Atmos. and Terr. Phys. 30*, 795-823.

Immel, T. J., S. B. Mende, M. E. Hagan, P. M. Kintner, and S. L. England (2009), Evidence of Tropospheric Effects on the Ionopshere, *EOS, 90*, 9, 69-80.

Kumar, V.V., M. L. Parkinson, P. L. Dyson, and G. B. Burns (2009a), Thunderstorm-associated responses in the vertical motion of the mid-latitude F-region ionosphere, *J. of Atmos. and Solar-Terr. Physics, 71*, 787–793.

Kumar, V.V., M. L. Parkinson, P. L. Dyson, and G. B. Burns (2009), The effects of thunderstorm-generated atmospheric gravity waves on mid-latitude F-region drifts, *J. of Atmos. and Solar-Terr. Physics, 71*, 1904-1915.

Lay, E. H. and X.-M. Shao (2011a), Multi-station probing of thunderstorm-generated D-layer fluctuations by using time-domain lightning waveforms, *Geophys. Res. Lett.*, *38*, L23806, doi:10.1029/2011GL049790.

Lay, E. H. and X.-M. Shao (2011b), High temporal and spatial-resolution detection of D-layer fluctuations by using time-domain lightning waveforms, *J. Geophys. Res., 116*, A01317, doi:10.1029/2010JA016018.

Lay, E. H., Shao, X.-M. & Carrano, C. S. (2013), Variation in total electron content above large thunderstorms, *Geophys. Res. Lett., 40*, 1945–1949, doi:10.1002/grl.50499.

Lyons, W. A., R. A. Armstrong, E. R. Williams, and E. A. Bering (2000), The hundred year hunt for the sprite. *Eos, Trans. Amer. Geophys. Union, 81*, 373–377.

Lyons, W. A., S. A. Cummer, M. A. Stanley, G. R. Huffines, K. C. Wiens, and T. E. Nelson (2008), Supercells and Sprites, *Bull. Amer. Meteor. Soc., 89*, 1165–1174, doi: 10.1175/2008BAMS2439.1

Marshall, R. A., and J. B. Snively (2014), Very low frequency subionospheric remote sensing of thunderstorm-driven acoustic waves in the lower ionosphere, *J. Geophys. Res. Atmos., 119*, 5037–5045, doi:10.1002/2014JD021594.

Seemala, G. K. & Valladares, C. E. (2011), Statistics of total electron content depletions observed over the South American continent for the year 2008, *Radio Sci., 46*, RS5019, doi:10.1029/2011RS004722.

Shao, X.-M., M. Stanley, A. Regan, J. Harlin, M. Pongratz, and M. Stock (2006), Total lightning observations with the new and improved Los Alamos Sferic Array (LASA), *J. Atmos. Oceanic. Technol*., *23*, 1273–1288.

Vadas, S. L., and D. C. Fritts (2004), Thermospheric responses to gravity waves arising from mesoscale convective complexes, *J. Atmos. Sol. Terr. Phys., 66*, 781–804.

Vadas, S. L., and H.-L. Liu (2013), Numerical modeling of the large-scale neutral and plasma responses to the body forces created by the dissipation of gravity waves from 6 h of deep convection in Brazil, *J. Geophys. Res. Space Physics, 118*, 2593–2617, doi:10.1002/jgra.50249.

Walterscheid, R. L., Schubert, G. & Brinkman, D. G. (2003), Acoustic waves in the upper mesosphere and lower thermosphere generated by deep tropical convection, *J. Geophys. Res., 108*(A11), 1392, doi:10.1029/2003JA010065.

Wiens, K.C., Hamlin, T., Harlin, J. & Suszcynsky, D. M. (2008), Relationships among Narrow Bipolar Events, "total" lightning, and radar‐inferred convective strength in Great Plains thunderstorms, *J. Geophys. Res., 113*, D05201, doi:10.1029/2007JD009400.

Wright, F. W., Jacchia, L. G. and Whipple, F. L. (1956), Photographic alpha-Capricornid Meteors, *Astron. J., 61*(2) 61-69.

Yue, J., S. L. Vadas, C.-Y. She, T. Nakamura, S. C. Reising, H.-L. Liu, P. Stamus, D. A. Krueger, W. Lyons, and T. Li (2009), Concentric gravity waves in the mesosphere generated by deep convective plumes in the lower atmosphere near Fort Collins, Colorado, *J. Geophys. Res., 114*, D06104, doi:10.1029/2008JD011244.

Yue, J., L. Hoffmann, and M. Joan Alexander (2013), Simultaneous observations of convective gravity waves from a ground-based airglow imager and the AIRS satellite experiment, *J. Geophys. Res. Atmos., 118*, 3178–3191, doi:10.1002/jgrd.50341.

Zettergren, M. D. & Snively, J. B. (2013), Ionospheric signatures of acoustic waves generated by transient tropospheric forcing, *Geophys. Res. Lett.*, **40**, doi:10.1002/2013GL058018.

Figures

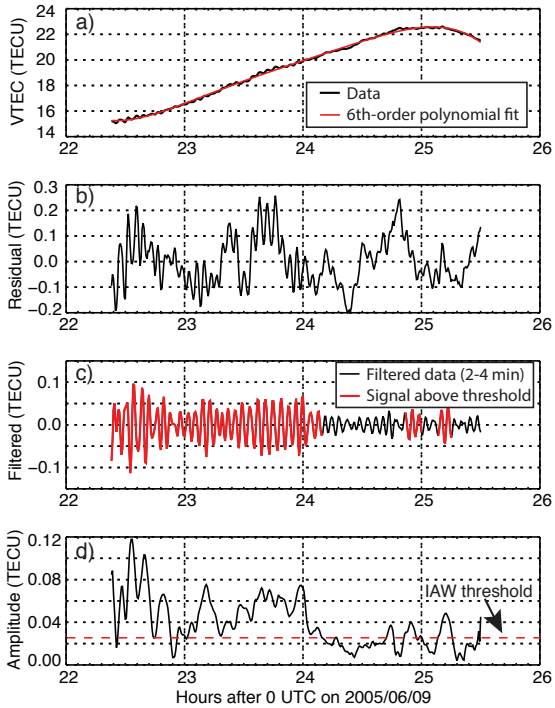


Figure 1. Example of data processing procedure to extract ionospheric acoustic waves from ground station okmu and GPS satellite PRN 20 on 09 – 10 June 2005. a) Vertical TEC (black) and best-fit 6$^{th}$-order polynomial (red). b) Residual after subtracting best-fit polynomial from data (removal of long-time scale variations). c) TEC variations after applying band-pass filter from 4.2 – 8.3 mHz. Red overlay highlights variations that surpass the 0.025 TECU IAW amplitude threshold. d) Analytic signal amplitude envelope of band-pass filtered TEC variations (black) and 0.025 TECU IAW threshold (red dashed).

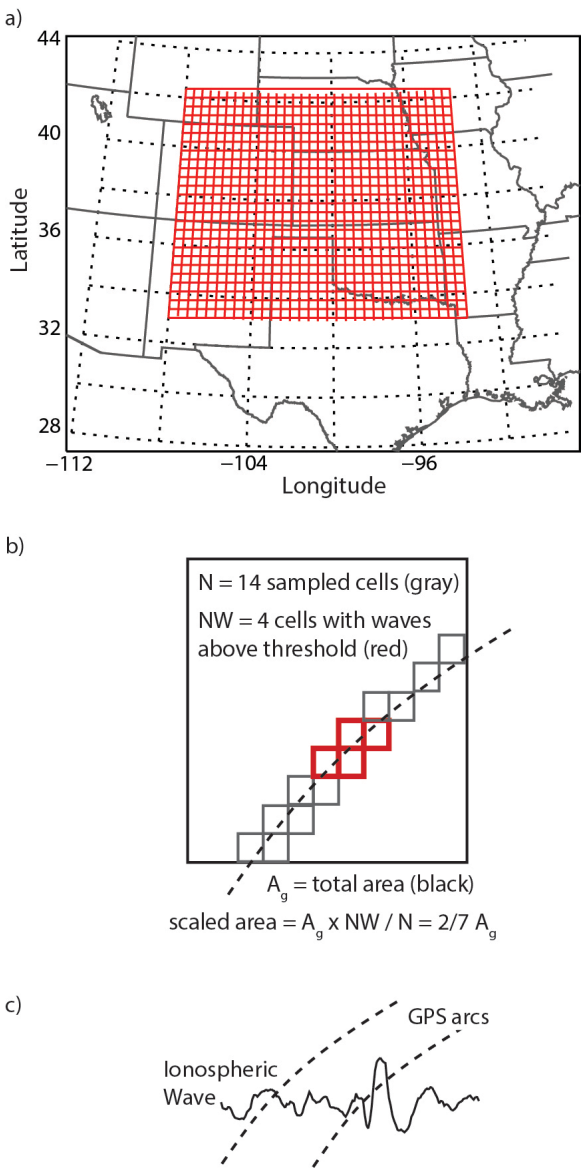


Figure 2. a) 40-km x 40-km spatial grid used for TEC statistical study. b) Cartoon of how scaled area is calculated. c) Illustration of detected maximum amplitude dependence on viewing geometry.

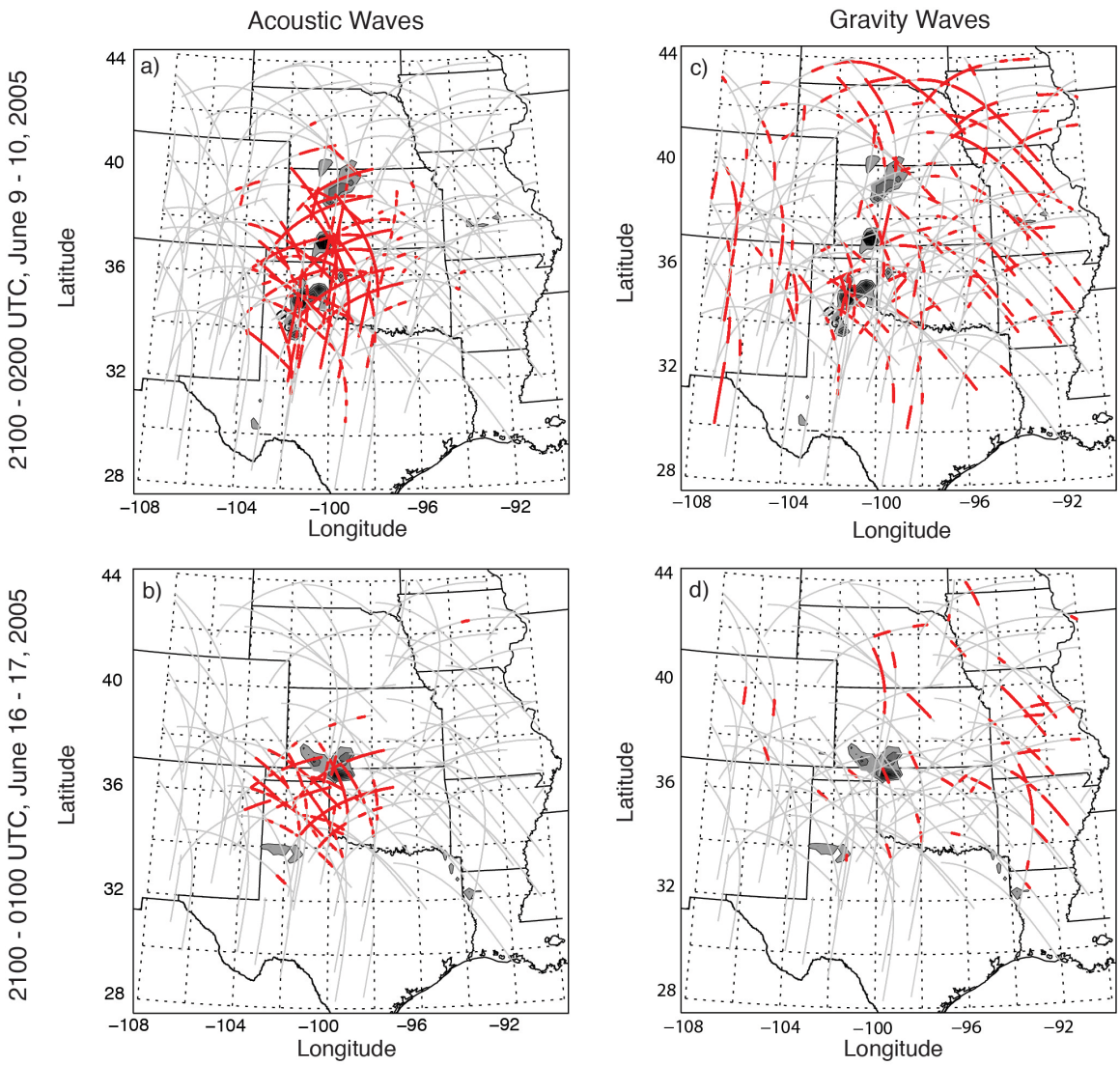


Figure 3. Maps of ionospheric acoustic waves (left) and gravity waves (right) near thunderstorms for 2100 – 0200 UTC on 9 – 10 June 2005 (top) and for 2100 – 0100 UTC, 16 – 17 June 2005 (bottom). Red points show where waves are above cutoff threshold (0.025 TECU for IAWs, 0.08 TECU for IGWs), gray points show ionospheric pierce points of sampled GPS paths, and black/gray contours show lightning activity.

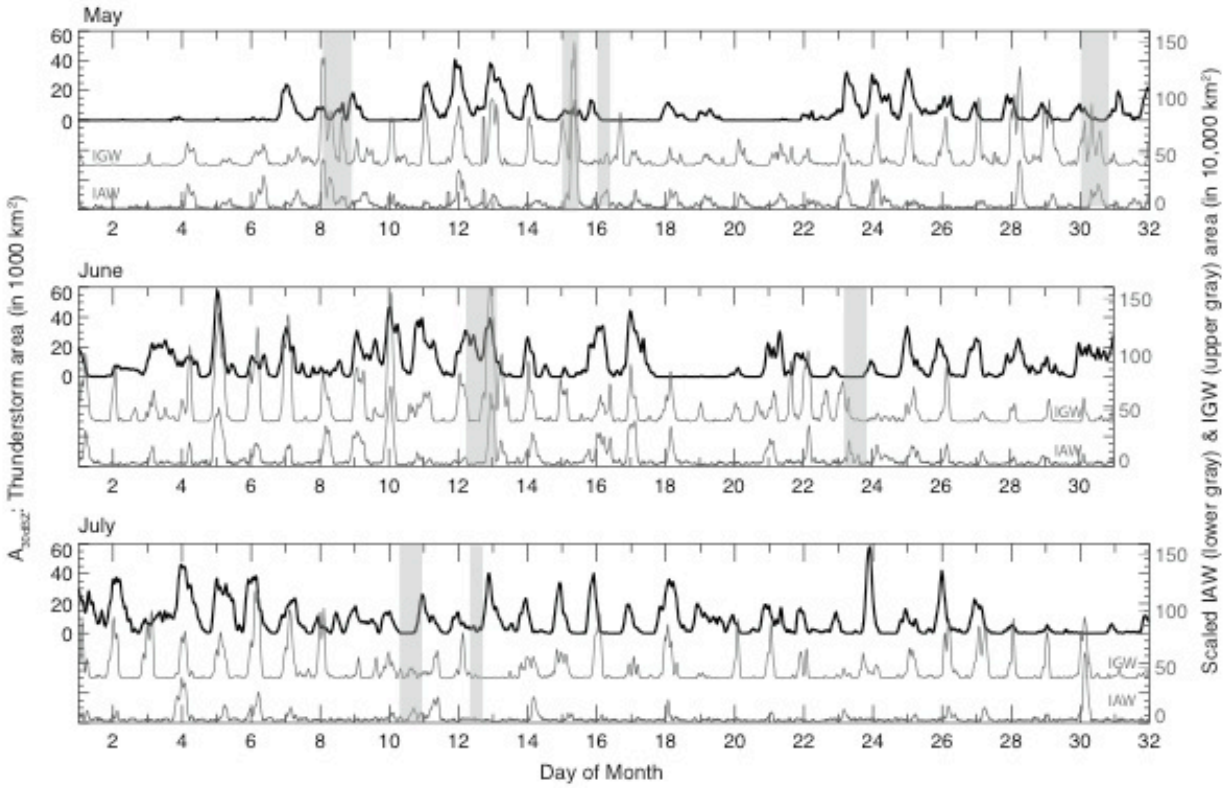


Figure 4. Time history of $A_{30dbz}$ (black; left-hand axis label), $A_{IGW}$ (upper gray), and $A_{IAW}$ (lower gray). $A_{IGW}$ and $A_{IAW}$ have been scaled by a factor of 10 compared to $A_{30dbz}$ (right-hand axis labels), and $A_{IGW}$ has been offset vertically by 400,000 km$^2$. Shaded regions are times with Kp > 5.3 that have been excluded from the remaining analyses in this paper.

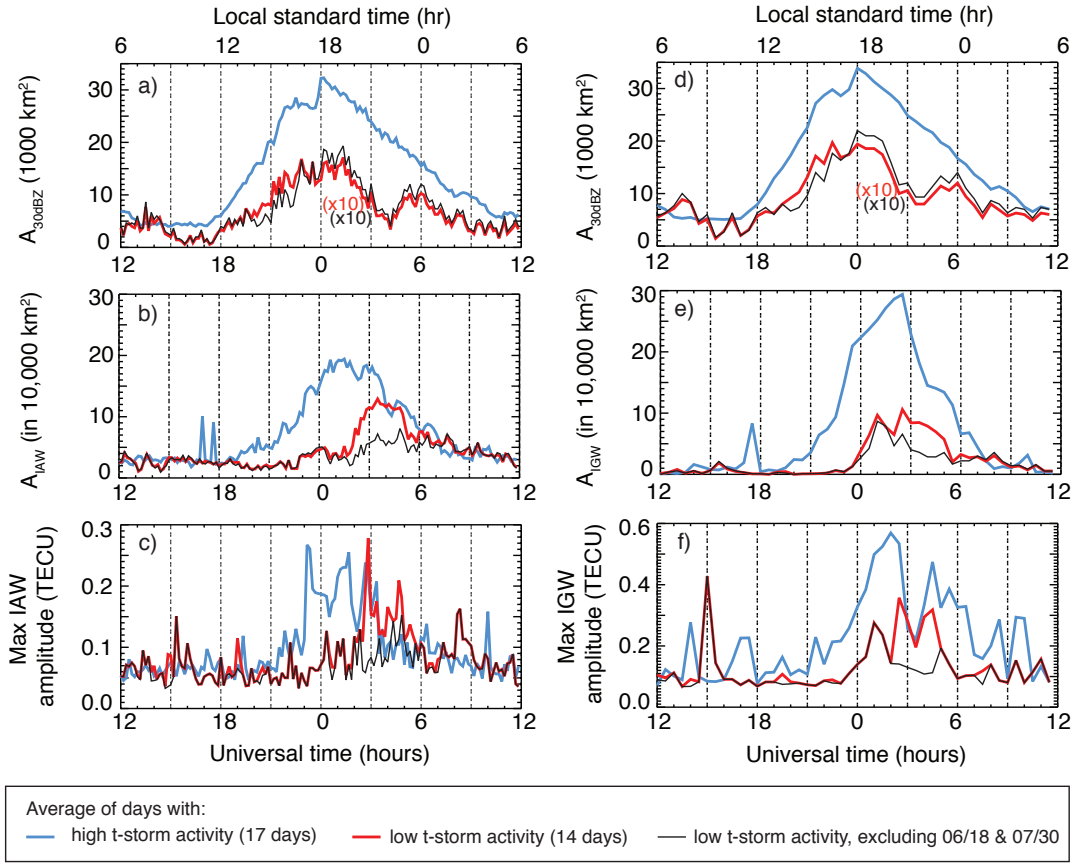


Figure 5. Diurnal averages of thunderstorm area (top row), ionospheric wave area (middle row), and maximum ionospheric wave amplitude (bottom row) for acoustic waves (left column) and gravity waves (right column). Days with Kp > 5.3 have been excluded from the averages. Blue curve averages only those days with $A_{30dbz}$ > 40,000 km$^2$ (high thunderstorm activity), and the red curve averages only days with $A_{30dbz}$ < 10,000 km$^2$ (low thunderstorm activity). The black curve also shows low thunderstorm activity average, but with June 18 and July 30 removed. Black and red curves in top row have been multiplied by 10.

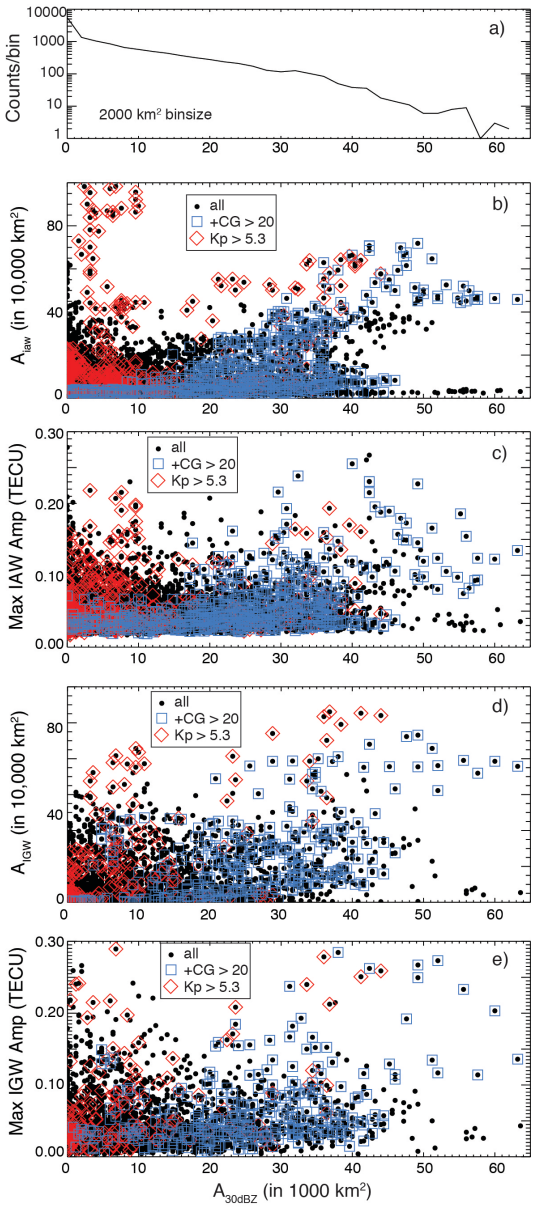


Figure 6. a) Histogram of thunderstorm area vs. total counts per 2000 km$^2$ bin. b) IAW area vs. thunderstorm area for each 10-minute period from Figure 4. c) Maximum amplitude of the IAW vs. thunderstorm area. d) $A_{IGW}$ vs. thunderstorm area. e) Maximum amplitude of the IGW vs. thunderstorm area. 10-minute periods with Kp> 5.3 are highlighted with red diamonds. 10-minute periods with > 20 +CGs are highlighted with blue squares.

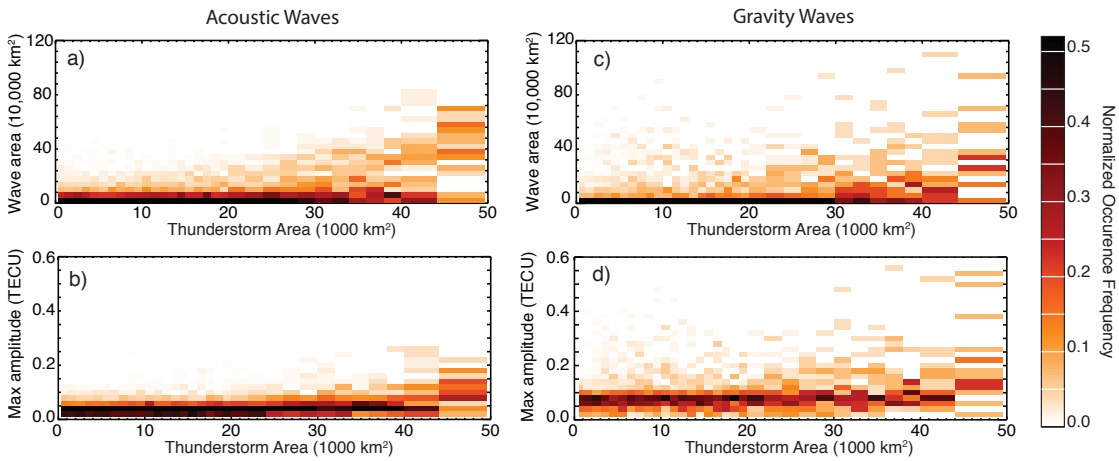


Figure 7. Normalized occurrence frequency of thunderstorm area vs. a) $A_{IAW}$, b) maximum IAW amplitude, c) $A_{IGW}$, and d) maximum IGW amplitude.

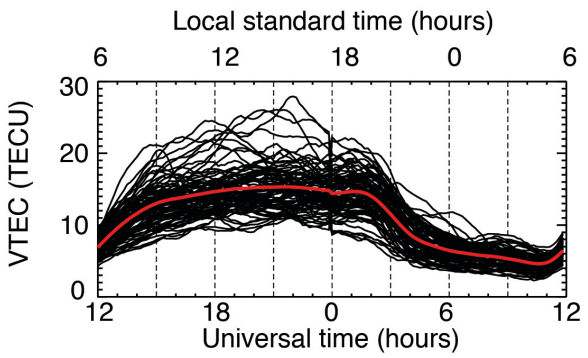


Figure 8. Daily vertical TEC measurements (black) and diurnal average (red).